Hindawi
Modelling and Simulation in Engineering
Volume 2024, Article ID 6151183, 13 pages
https://doi.org/10.1155/2024/6151183

Research Article

Predictive Modeling of Environmental Impact on Drone Datalink Communication System

I. Bennageh,[1] **H. Mahmoudi**,[1] **H. Hajjaji**,[2] **I. Laabousse**,[3] **and A. Hamdouchi**[4]

[1]*Department of Power Electronics, Mohammadia School of Engineers, Mohammed V University in Rabat, 10090 Rabat, Morocco*
[2]*Department of Embedded Systems, Faculty of Science and Technology, Sidi Mohammed Ben Abdellah University, 30050 Fez, Morocco*
[3]*Laboratory of Engineering Sciences, National School of Applied Sciences, Ibn Tofail University, 14020 Kenitra, Morocco*
[4]*Department of Vanguard, Mohammed VI Polytechnic University, Ben Guerir 43150, Morocco*

Correspondence should be addressed to I. Bennageh; imranebennageh@research.emi.ac.ma

Received 18 January 2024; Revised 12 March 2024; Accepted 15 March 2024; Published 4 April 2024

Academic Editor: Franco Ramírez

In this study, we introduce an innovative model for evaluating the impact of environmental factors on drone-to-ground control station datalink communications. Our approach integrates both deterministic and stochastic processes to account for small-scale and large-scale fading effects, encompassing propagation attenuation, the Rician fading model, and Gaussian noise to accurately reflect real-world conditions. The model is implemented on signals transmitted using spread spectrum modulation. Through a comparative analysis of the model's predictions against actual signals received in three distinct environments, the model's efficacy in diverse scenarios is affirmed. Error metrics obtained from Monte Carlo simulations are employed to validate the theoretical results against experimental data. The proposed approach is pivotal for predicting the transmission range and understanding the electromagnetic susceptibility of the datalink, offering a substantial contribution to the optimization of remote drone control.

1. Introduction

Generally, drone control is achieved through a radio link in the line-of-sight (LOS). This direct link is often subject to electromagnetic perturbations in the operating environment of drones. These interferences may originate from both natural and artificial sources. This noise can arise from various sources, including transient electromagnetic fields, jamming, signal attenuation, continuous random noise, Gaussian noise, and multipath fading. The analysis of environmental interferences through modeling enables the anticipation of both the datalink strength and the drone's control range.

Numerous investigations have been undertaken to assess how external environmental interferences impact the datalink of drones. The majority of these studies, employing either statistical [1] or deterministic methods [2] or a combination thereof [3], conduct virtual simulations or rely solely on analytical outcomes. They often rely on virtual simulations or strictly on analytical outcomes.

Recent trends in signal propagation research focus on predicting signal fading using a variety of methods, as referenced in [4–6]. These methods are predominantly characterized by the application of statistical analysis or, in the case of the most recent studies, artificial intelligence. Furthermore, to circumvent the issue of signal fading entirely, recent advancements have been directed towards incorporating free-space optical (FSO) communication techniques into drones, as discussed in [7, 8]. However, the practical implementation of FSO technology in drones presents its own set of challenges. Precise alignment between the transmitting and receiving ends is crucial, which poses significant difficulties in dynamic environments typical for drone operations. Moreover, the efficiency of FSO systems can be adversely affected by atmospheric conditions such as fog, rain, and

dust. Despite these obstacles, innovative solutions are emerging, with studies in [9, 10] offering promising approaches to mitigate these challenges.

In drone applications, path loss prediction and channel models represent active research topics as highlighted by the survey [11]. A lot of studies usually adopt either the path loss [12] of the drone datalink or the channel in which the drone operates [13] to predict the datalink behavior. For instance, Bing [14] modeled both the large-scale and small-scale fading with only the channel modeling while Perotoni et al. [15] proposed a tool for modeling the propagation of drone datalink. In recent researches, these modeling environments are incorporated into embedded devices to facilitate the analysis and prediction of radio signal path loss in unmanned aerial vehicle (UAV) communication scenarios such as the UAVRadio Python module proposed by [16].

The distinctiveness of our model lies in the use of path loss fading alongside the channel modeling. Indeed, these two models operate at different levels of communication system analysis. Path loss focuses on the physical aspects of radio wave propagation between antennas over a given distance, while the channel model applies at a more abstract level to represent the effect of any communication channel on a signal.

Although they are different, these models are complementary in the analysis and design of communication systems. Path loss is used to estimate the initial signal power required at the transmitter or to design antennas based on transmission distance and power requirements at reception. The channel model is then utilized to analyze how the transmitted signal is affected by the specific channel (including the effects of propagation modeled by Friis) and by noise, to optimize error detection and correction at the receiver.

Interferences primarily stem mostly in drone application from path loss attributed to signal propagation [17], external noise sources [18, 19], or obstacles in the environment that cause multipath fading [20].

In this research, we analyze path loss by treating it as a deterministic factor in signal fading, utilizing the Friis transmission formula to quantify signal attenuation. We address the inherent variability in signal transmission through stochastic models, specifically incorporating additive white Gaussian noise (AWGN) to simulate the random interference that affects signals in real-world communication scenarios. Furthermore, we explore the impact of multipath fading (stemming from reflections, diffractions, and scattering caused by physical obstructions) on the datalink from the control station to the drone's receiver. The multipath fading is also considered a stochastic model and can be expressed by the Rician fading. In fact, the drone's transmission is primarily within the line-of-sight. By integrating these three attenuation models (Friis transmission, AWGN, and Rician fading), we aim to provide a comprehensive estimate of the received signal power in specific environments.

The remainder of this paper is organized as follows. Section 2 discusses the drone's datalink and presents the test bench for conducted and radiated emission measurements. In Section 3, we provide an overview of the fading types that can encounter drone communications. Further details regarding the fading types applied in the test environments are provided. In Section 4, we apply the fading signal model obtained to a signal emitted by a transmitter using spread-spectrum modulation. In the same section, we compare the theoretical results obtained using the Monte Carlo simulation with the experimental results. In conclusion, we present the outcomes of this novel model, articulate the key findings, and thereby pave the way for future enhancement and development.

2. Description of the Test Bench

2.1. Datalink. Datalink communication in drones is a crucial element that plays a critical role in the operation and control of unmanned aerial vehicles (UAVs). There are several types of drone datalink systems as stated in [21, 22]. The most important one is the command datalink. This datalink functions as the communication link between the drone and its ground control station (GCS), facilitating the real-time exchange of vital information, such as telemetry data, commands, and video feeds. These communication systems are designed to establish reliable and secure connections, enabling operators to remotely pilot and monitor drone performance. The success of a drone's mission, whether it involves surveillance, reconnaissance, or other applications, depends heavily on the strength and efficiency of the datalink. Advanced datalink technologies incorporate features such as frequency-hopping, encryption, and error-correction mechanisms [23] to ensure secure and interference-resistant communication. As the drone industry continues to advance, research and progress in datalink technologies are crucial for enhancing the overall capabilities, safety, and reliability of unmanned aerial systems.

In our case, we utilize a command datalink that relies on modulation using the frequency-hopping spread spectrum (FHSS). This type of datalink has been proven to be particularly resistant to various environmental perturbations. Despite its performance, interference from different sources significantly reduces the communication range. Consequently, modeling the environment based on communication type allows us to determine the performance of the employed datalink.

To ensure seamless integration of our model with real-world scenarios, we have developed a specialized test bench to evaluate the command datalink under various environmental conditions. The subsequent section describes this setup, highlighting its deployment across three distinct testing grounds, chosen for their relevance to UAV operational environments.

2.2. Test Bench Description. The proposed test bench can be installed in various operational environments for drones. This environment could be an obstacle-free field, an urban area, around high-tension power lines, an area with strong electromagnetic interference, or inside a building.

The test bench was placed in three different environments: a laboratory room at the basement of the university, an open area without any obstacle around, and in the forest with several physical obstacles.

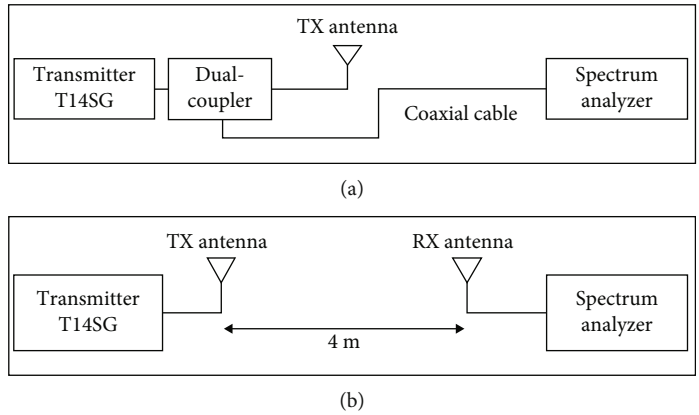

Figure 1: Conducted and radiated emission test bench diagram: (a) diagram for conducted measurement; (b) diagram for radiated measurement.

The test bench essentially comprises

(i) spectrum analyzer Anritsu MS2711E model, covering the frequency range from 9 KHz to 3 GHz

(ii) log-periodic antenna LP-02 NARDA with a gain of 6 dBi

(iii) dual directional coupler 778D Keysight

(iv) T14SG transmitter Futaba using 14-channel frequency-hopping technique in 2.4 GHz

All the equipment used is calibrated and up to date.

The measurements performed are primarily based on the general instructions described in the U.S. military standard Mil-Std-461G [24], specifically the conducted emission with antenna port (CE106 in the standard) and radiated emissions, antenna spurious, and harmonic outputs (RE103 in the standard).

The two types of measurements were performed following the diagrams in Figure 1. In the conducted measurement (Figure 1(a)), the antennas of the transmitter and receiver (spectrum analyzer antenna) were substituted with a well-shielded coaxial cable (Figure 2).

In the radiated measurement (Figure 1(b)), the transmitter was placed on a wooden table at three different environments. The spectrum analyzer gathered the radiated emissions through the antenna. In Figure 3, the test was conducted in the university laboratory basement with a distance of 4 m from the receiving antenna connected to the spectrum analyzer. In Figure 4, the test was conducted in an open area far away from any RF source or obstacle with a distance of 10 m from the receiving antenna. In Figure 5, the test was conducted in a forest where there are several obstacles around and with a distance of 20 m from the receiving antenna.

The obtained model will be tested in the 3 different configurations to test its efficiency with a maximum of parameters available in static mode. The aim is not to draw comparisons among the three environments; rather, it is to contrast the theoretical outcomes with the experimental ones, considering various parameters, hence the choice of 3 different distances.

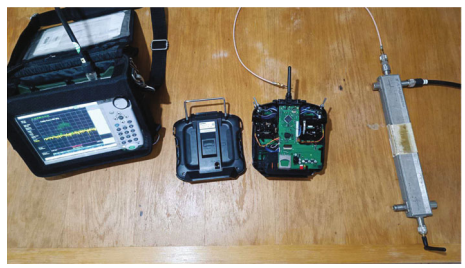

Figure 2: Conducted emission measurement of the transmitter T14SG.

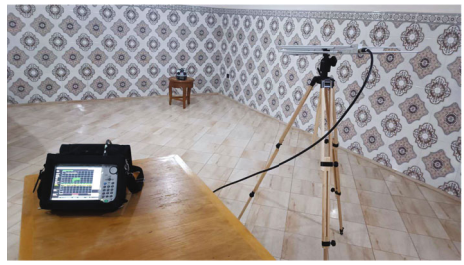

Figure 3: Radiated emission measurement in the laboratory basement (4 m between the transmitter TX and the receiver RX).

For the 4 measurements (one conducted and three radiated), the same spectrum analyzer parameters were applied (span, reference level, sweep time, detection mode, resolution bandwidth, video bandwidth, etc.).

It is noteworthy that the conducted test measurement should be performed in an environment without electromagnetic interference, ideally in an anechoic chamber. In the absence of this facility, a special shielded coaxial cable is used to enable interference-free communication.

Note that in other cases where the transmission ground station has a fixed nonremovable antenna, the same signal from the transmitter can be reproduced using an arbitrary waveform generator (AWG). The reproduced signal can be then measured by the spectrum analyzer by means of coaxial cable. This generator can replicate almost any signal by providing the exact data of a desired signal.

Figure 4: Radiated emission in open test area (10 m between the transmitter TX and the receiver RX).

2.3. Fading Modeling. The main idea is to process the conducted signal in Figure 1(a) based on the environmental data in Figure 1(b) to obtain a theoretical radiated signal at the receiving antenna. This theoretically received signal is then compared to the experimentally received signal in Figure 1(b). Analyzing the situation, the signal emitted from the transmitter goes through the following steps:

(i) The signal is converted into an electromagnetic field by the transmitter antenna

(ii) The radiated emitted signal undergoes path loss attenuation due to the distance propagation

(iii) The emitted signal undergoes reflection, diffraction, and scattering owing to multipath fading

(iv) Environmental noise adds to the emitted field

The field received by the receiving antenna is transformed into an electrical signal and then introduced to the spectrum analyzer through internal filters for measurement and display.

The convolution of these different phenomena produces a radiated field. The conducted signal was processed following the aforementioned steps to obtain results similar to those measured experimentally.

2.4. Transmission Hardware. The T14SG transmitter transmits control data in a frequency band between 2405.376 MHz and 2477.056 MHz using Frequency Agile Spread Spectrum Technology (FASST). It is a proprietary radio transmission protocol developed by Futaba for use in radio control systems. FASST is a more expensive protocol with less latency and a much greater range than the classical frequency-hopping spread spectrum (FHSS).

The spectrum analyzer was configured to capture signals from 2300 to 2600 MHz. For each test, 551 power measurement samples were taken in this 300 MHz bandwidth. The focus here is not to detect spurious signals outside the transmission domain in a large bandwidth but rather to process the useful control data, hence the choice of the configured frequency band.

3. Fading Experience for Drone

3.1. Fading Types. In drone communication systems, the exploration of fading phenomena is essential for improving the reliability and performance of the wireless links. Fading, characterized by fluctuations in the signal strength during transmission, is a phenomenon that is influenced by various environmental factors. There are two major types of fading, the large-scale and small-scale fading. Large-scale fading, associated with gradual changes in signal strength, holds particular significance in drone applications, where the terrain and surrounding obstacles can lead to sustained alterations in communication quality. Conversely, small-scale fading, marked by rapid signal fluctuations, is closely tied to the dynamic movement of drones and multipath directions of the signal, causing abrupt changes in the signal propagation path. Investigating these fading types is crucial for developing robust communication protocols and adaptive systems that can effectively address the challenges posed by the unpredictable and dynamic nature of a drone's operational environment. Several types of signal fading [25] can be distinguished, as shown in Figure 6.

In our scenario, the fixed-wing drone is in LOS with the transmitter at a known distance (4 m for the basement, 10 m in open area, and 20 m in the forest). Shadowing attenuation is not considered in the large-scale fading branch. In addition, because the transmission and reception antennas are static, we can deduce the absence of the Doppler effect. However, frequency-selective fading is noted, which is a more precise model of multipath fading than the flat fading model. Hence, the control signal undergoes attenuation in both path loss and multipath fading.

In our tests, despite the fixed-wing drone's static LOS with the transmitter, our results accounted for both large-scale path loss and frequency-selective fading. These findings set the stage for a deeper examination of path loss, which we explore next in the context of the generalized Friis formula and its practical implications in our experimental setup.

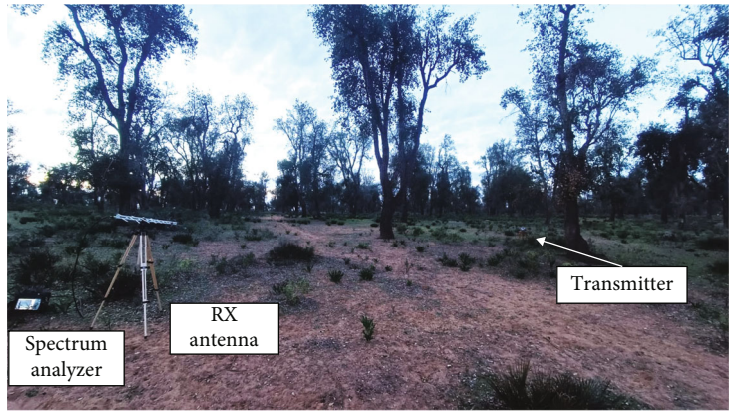

Figure 5: Radiated emission measurement in the forest (20 m between the transmitter TX and the receiver RX).

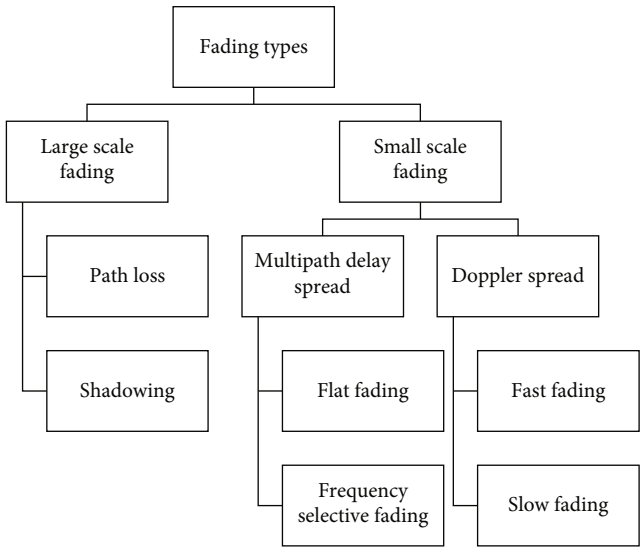

Figure 6: Fading types.

3.2. Path Loss Fading. Telecommunications engineering states that the power density of an incident field from a radio transmitter undergoes attenuation owing to phenomena such as free-space propagation, presence of obstacles, and antenna losses (impedance, polarization, and directivity). The attenuations recorded in the communication between two antennas separated by the distance R are summarized by the generalized Friis formula:

$$\frac{P_r}{P_t} = G_t G_r \left(1 - |s_{11}|^2\right)\left(1 - |s_{22}|^2\right) \cdot \left|\vec{u} \cdot \vec{v}\right|^2 \cdot \left(\frac{C}{4\pi R f}\right)^2, \quad (1)$$

where $P_{r/t}$ represents the received/transmitted power, $G_{r/t}$ denotes the gain of the receiving/transmitting antenna, and s_{11} and s_{22} are the reflection coefficients of the transmitting and receiving antennas, respectively. The scalar $|\vec{u} \cdot \vec{v}|$ denotes the term related to the antennas mismatch. For testing purposes, the antennas are well polarized ($|\vec{u} \cdot \vec{v}| \approx 1$) and adapted according to a common impedance of 50 Ω ($|s_{11}|^2 = |s_{11}|^2 \approx 0$) to simplify the formula. Note that the losses due to multipath fading are modeled in the next section. The insertion losses of the coaxial cable were retrieved from the calibration test report and considered.

First, we calculate the effective emitted power of transmitter T14SG starting from the power data displayed on the spectrum analyzer in Figure 1(a), following these steps:

(i) The amplitude of the power read on the spectrum analyzer is the first data to be considered ($P'_{t,dB}$)

(ii) The input attenuation of the spectrum analyzer filter (5 dB) is added

(iii) The insertion losses related to the used cable (0.6 dB) are added

(iv) Attenuation of the directional coupler (20 dB) is added. The directional coupler lowers the transmitter signal power to protect the input filters of the frequency analyzer

The obtained result represents the effective transmitted power of the signal emitted by the T14SG transmitter; thus, $P_{t,dB} = P'_{t,dB} + 25.6$.

To obtain the theoretical power density of the signal at the receiving antenna, such as in the experiment in Figure 1(b), the emitted signal from the transmitter T14SG undergoes the following:

(i) Gain G_t of the transmitting antenna: it is assumed that the losses due to antenna mismatch are nearly zero

(ii) Attenuation due to propagation in free space: the antennas are in line-of-sight

(iii) Reception of the incident power field by the receiving antenna with a gain G_r

The operations outlined above regarding attenuation due to propagation allow us to simplify Equation (1) into its logarithmic form:

$$P_{\mathrm{r,dB}} = P'_{\mathrm{t,dB}} + G_{\mathrm{r,dB}} + G_{\mathrm{t,dB}} + 20 \cdot \log_{10}\left(\frac{C}{4\pi R f}\right) + 25.6. \quad (2)$$

To obtain the theoretical power of the received signal, one must consider the power losses due to multipath fading, as well as the noise present in the environment.

3.3. Multipath Fading. Multipath fading occurs when signals transmitted to the drone experience multiple reflections and refractions as they interact with obstacles or the Earth's surface, resulting in variations in the signal strength and phase at the receiver. Understanding and mitigating the effects of multipath fading are of paramount importance in drone applications, where high reliability and low-latency communication are essential. Addressing the impact of multipath fading in drone communication systems is pivotal for improving the capabilities and reliability of UAVs in diverse applications.

To describe multipath fading, several statistical models exist that best capture the observed phenomenon. Examples include Rayleigh fading, Rician fading, Nakagami fading, and Weibull fading.

The model best suited to our situation is Rician fading. This model is applied when there is a strong line-of-sight signal component in the presence of other scattered components from different paths and reflecting obstacles in the environment.

It is crucial to understand the model's dependency on a strong line-of-sight (LOS) component for accurately modeling signal transmission in diverse environmental conditions with Rician fading model. While the model provides a robust framework for scenarios with a clear LOS path, its efficacy diminishes in environments where the LOS component is weak or obstructed, leading to a scenario where the scattered components predominate. Such conditions are not uncommon in urban or heavily built-up areas, where buildings and other structures can significantly interfere with the signal path. In these cases, the proposed model may not fully capture the complexity and variability of real-world signal behavior, necessitating the consideration of alternative fading models like Rayleigh, Nakagami, or Weibull. These models offer a more nuanced understanding of signal transmission in environments characterized by nondominant or absent LOS components, providing a complementary perspective to the limitations of the current approach.

3.4. Rician Fading. The Rician fading distribution provides an appropriate representation of the variations in the signal envelope within narrowband multipath fading channels, characterized by a clear LOS path connecting the transmitter and the receiver. This is a statistical representation that models the effects of multipath propagation in a wireless communication channel, which is our case. The Rician probability density function is as follows:

$$f(z) = -\frac{z^2}{\sigma^2} e^{-\left(z^2+\nu^2\right)/2\sigma^2} I_0\left(\frac{z\nu}{\sigma^2}\right), \quad (3)$$

where I_0 is the modified Bessel function of the first kind with a zero order, ν^2 is the LOS component, and $2\sigma^2$ is the non-LOS component.

The Rician distribution is often represented by its K -factor defined by

$$K = \frac{\nu^2}{2\sigma^2}. \quad (4)$$

According to [26, 27], the received signal $Y(t)$ through the Rician channel from a transmitted signal $x(t)$ can be expressed as follows:

$$Y(t) = h(t) \otimes x(t) + n(t), \quad (5)$$

where $n(t)$ is the noise and $h(t)$ is the complex response of the Rician channel. In the integral form, the received signal in time domain can be expressed by

$$Y(t) = \int_{-\infty}^{+\infty} h(\tau) x(t-\tau) d\tau + n(t). \quad (6)$$

The complex expression of the Rician channel response h is deduced from [28, 29]

$$h = Ae^{-j2\pi\theta} + \sum_{i=1}^{N} a_i e^{-j2\pi\phi_i}, \quad (7)$$

where $A \geq 0$ is the magnitude of the direct path of the signal communication, θ is the corresponding phase shift caused by the transmission distance and can uniformly take any value in $[0, 1]$, a_i are the amplitudes of the scattered waves, and ϕ_i are their respective phase shifts. The sum is over N paths of the scattered waves. Each of these scattered paths possesses a comparable strength but is noticeably weaker than the direct path.

Equation (7) of the Rician response channel can be developed in another form by introducing the Rician K -factor according to [20]:

$$h = \sqrt{\frac{K}{K+1}} h_{\mathrm{LOS}} + \sqrt{\frac{1}{(K+1)}} h_{\mathrm{NLOS}}, \quad (8)$$

where the NLOS component $h_{\mathrm{NLOS}} \sim \mathcal{N}_{\mathbb{C}}(0\,;1)$. This complex Gaussian distribution is motivated by the central limit theorem, which states that the sum of several independent and identically distributed random variables is approximately Gaussian.

$h_{\mathrm{LOS}} = e^{-j2\pi\theta}$ and $\theta \sim \mathcal{U}(0, 1)$ are the phase shift uniform random variables.

Note that in many studies, the LOS component is mentioned as a deterministic value, as in [26]. However, it was demonstrated in several new research works, such as [29], that the LOS component h_{LOS} has a phase shift that follows a uniform random value $\mathcal{U}(0, 2\pi)$, which will be considered for this study.

3.5. Rician Channel Response in Frequency Domain. The aforementioned Rician distribution model was expressed in the time domain. In order to use the power data measured by the frequency analyzer, we must convert the time domain model to the frequency domain through Fourier transformation. Furthermore, by using the frequency domain, the convolution product in Equation (6) becomes a simple multiplication. Equation (5) becomes

$$Y(f) = H(f) \cdot X(f) + N(f),$$
$$Y(f) = \left(\sqrt{\frac{K}{K+1}} \cdot e^{-j2\pi\theta} + \sqrt{\frac{1}{(K+1)}} h_{\mathrm{NL}} \right) \cdot X(f) + N(f), \tag{9}$$

where $h_{\mathrm{NL}} \sim \mathcal{N}_{\mathbb{C}}(0\,;1)$ is a random normal complex variable and $N(f) \sim \mathcal{N}_{\mathbb{C}}(0\,;N_0)$ is a random Gaussian variable. N_0 represents the noise power spectral density.

Because this model concerns the transmission channel related to the test environment, we must use the radiated measurement power data in Figure 1(b) to estimate the K-factor used in frequency Rician channel response $H(f)$.

Note that estimating the K-factor is a delicate exercise and continues to be the subject of several studies, such as those in [30–33].

In this study, we used the computed LOS component and the measured received power (LOS + NLOS) in Figure 1(b) to estimate the K-factor over the bandwidth considered. Thus, we obtain

$$K = \frac{1}{N+1} \sum_{i=0}^{N} \frac{P_{\mathrm{LOS}}}{P_{\mathrm{LOS+NLOS}} - P_{\mathrm{LOS}}}, \tag{10}$$

where $P_{\mathrm{LOS+NLOS}}$ is the power measured in Figure 1(b) and P_{LOS} is the determinist LOS power calculated in Equation (2) without considering the multipath fading. The K-factor is obtained by calculating the average over the N measurement samples across the considered frequency bandwidth.

3.6. Multipath Fading of the Conducted Measured Signal. The power measured by the frequency analyzer is an averaged power over the RBW (resolution bandwidth); thus, we got in frequency domain the averaged received power spectral density (PSD) in

$$\frac{Y^2(f)}{2} = H^2(f) \cdot \frac{X^2(f)}{2} + X(f)N(f) + \frac{N^2(f)}{2}, \tag{11}$$

where $|P_t(F)| = \int_F^{F+\mathrm{RBW}} ((X^2(f))/2)\, df$ is the conducted power of transmitted signal measured by the spectrum analyzer in Figure 1(a) (see Section 3.2). $|P_h(F)| = \int_F^{F+RBW} ((Y^2(f))/2)\, df$ is the received power in the considered Rician channel.

3.7. Noise Measurement. In drone applications, the presence of noise poses a significant challenge that can affect the reliability and precision of various functionalities. Noise in drone applications can originate from diverse sources, including sensor inaccuracies, environmental conditions, and electronic interference [6]. Accurate modeling of this noise is important for enhancing the performance of drone systems. Statistical models offer a systematic approach for characterizing and understanding the stochastic nature of noise in drone applications. By employing generalized statistical models [34], researchers have aimed to capture the variability and randomness associated with different noise sources following the environment specificity. For instance, Gaussian models are commonly used to represent additive noise, whereas more complex models exist and may be employed to simulate specific environmental conditions. These statistical models enable researchers and engineers to assess the impact of noise on drone operation, refine control algorithms, and develop strategies to mitigate the adverse effects of noise.

The noise considered in Equation (5) is modeled as additive white Gaussian noise (AWGN). It is important to note that, in practice, "white" noise possessing an infinite bandwidth is an idealization. In real-world communication systems, the bandwidth is finite, and thus, the spectrum of the noise is limited to this bandwidth. Nevertheless, the AWGN model is employed as an effective approximation for a wide range of frequencies within the system's operational bandwidth. The statistical properties of AWGN, particularly its mean and variance, are crucial for predicting the performance of communication channels, designing error-correction codes, and assessing the overall reliability of the communication system in the presence of noise. The use of the AWGN model in this context is a standard approach in the analysis of communication systems and is intended to represent the combined effect of many random noise sources found in typical operating environments.

Hence, the noise power within the datalink bandwidth was measured on the receiving antenna. Noise listening was recorded in the test environments without any transmission operations to capture fluctuations in noise power. These data are transmitted to the MATLAB tool to determine the statistical parameters of AWGN, namely, the average transmitted power and its statistical variance relative to this average.

For all measurements in the three environments studied (basement, forest, and open area), we have recorded the background signal present with the transmitter turned off. A goodness-of-fit test is applied in MATLAB to confirm the noise characterization, namely, mean and variance.

In general communication systems and signal processing theory, the assumption of zero mean for AWGN simplifies the analysis and aligns with the idea that noise is equally likely to be positive or negative and has no systematic bias. However, in some specific cases or models, noise with a nonzero mean may be considered. Because the measurement is conducted with a spectrum analyzer that gives the received signal a certain amplification with its filters, we consider the mean to be a nonzero value.

These parameters are used to generate the noise power with the simplest statistical formula:

$$N = \sqrt{N_0} \cdot Z, \tag{12}$$

where $Z \sim \mathcal{N}_{\mathbb{C}}(0\,;1)$ is a complex normal Gaussian random variable and N_0 is the power spectral density of the noise.

4. Results and Discussion

4.1. Conversion to Frequency Domain. In this study, we recorded measurements of conducted emissions, radiated emissions, and environmental AWGN using the frequency analyzer. These measurements were then diligently structured into tabular arrays, facilitating their integration and subsequent manipulation in MATLAB. This step is crucial for the ensuing analysis, which necessitates a transition of all data from the time domain into the frequency domain, encompassing the Rician channel response as well as the associated noise profile.

The Fourier transform, renowned for its extensive applicability and simplicity of execution within MATLAB, was the transformation technique of choice. It is important to note, however, that the MATLAB FFT (fast Fourier transform) algorithm assumes the signal to be periodic, which conflicts with the characteristics of the spread spectrum modulation used in this context. To reconcile this and utilize the FFT algorithm effectively, we applied a Hamming window. This approach accommodates the nonperiodic nature of both the channel response h and the noise, ensuring a smooth and accurate transformation into the frequency domain for our analysis.

4.2. Theoretical Received Power. It should be noted that the theoretical power supposed to be received by the receiving antenna of the spectrum analyzer arises from the emitted conducted power in Figure 1(a) and undergoes the following attenuations:

(i) Path loss due to free-space propagation between the two antennas

(ii) Attenuation due to the multipath fading phenomenon

(iii) Gaussian noise in the working environment

From Equation (2) and Equation (11), the final logarithmic format of the power vector is deduced as follows:

$$P_{\mathrm{r,dB}} = 10 \cdot \log_{10}(|P_h|) + G_{\mathrm{r,dB}} + G_{\mathrm{t,dB}} + 20 \cdot \log_{10}\left(\frac{C}{4\pi R f}\right) + 25.6. \tag{13}$$

4.3. Monte Carlo Simulation. Given the stochastic nature of the proposed model, each execution of the corresponding MATLAB script yields different results. This variability is intrinsic to models that incorporate random elements or are influenced by probabilistic factors, reflecting real-world conditions where slight changes can lead to different outcomes.

To enhance the robustness and reliability of our results, we will employ the Monte Carlo simulation method. This approach will allow us to perform a large number of trials with the model, which helps in capturing a broader spectrum of possible outcomes and provides a more comprehensive statistical analysis. By aggregating the data from these numerous simulations, we can determine a more accurate and dependable representation of the model's predictions.

The Monte Carlo method is particularly beneficial because it does not rely on a single set of results; instead, it considers the variability and uncertainty inherent in the model to predict a range of possible outcomes. This will enable us to derive meaningful insights and more useful data, as we can statistically quantify the confidence in our model's predictions and better understand the probability distribution of the potential results. Upon executing the MATLAB code with a varying number of simulations, we observe that the error metrics (discussed in the Section 4.4) stabilize after reaching a threshold of 50,000 simulations.

Note that 50,000 simulations are mentioned to ensure that anyone wishing to replicate the simulation using the MATLAB code can achieve stable values to the nearest thousandth of a dB for both mean absolute error (MAE) and mean squared error (MSE) (discussed later in this paper). However, this increases the program's execution time to about 17 seconds. 5000 simulations could also achieve stable values to the nearest hundredth in less than 1 second.

While running the program on a PC does not present a significant time constraint, if the program is to be deployed on a drone, the number of simulations must be adjusted based on the embedded system's processing speed to allow for real-time operation by the drone.

4.4. Results and Discussion. In Figure 7, we plot the radiated power field emitted by the transmitter, recorded experimentally at the receiving antenna of the frequency analyzer (Figure 1(b)), along with the conducted emitted power (Figure 1(a)). The observed difference between the two traces indicates that the power emitted by the transmitter undergoes significant attenuation and distortion when irradiated in the test environment.

The measured conducted signal experiences attenuation due to free-space propagation. By computing the theoretical received signal by only considering the path loss (large-scale fading) in the basement environment, we obtain the plotted curves in Figure 8. Also, a significant difference was observed between the two curves. We conclude that the small-scale fading plays a critical role in the signal attenuation and should be considered.

After accounting for multipath fading and the noise effect, the signals shown in Figures 9–11 were obtained using the statistical model in MATLAB. It is concluded that this theoretical model closely aligns with the data measured in practice using a frequency analyzer. To quantify the discrepancy, we will proceed with a comparative analysis using location-based error metrics, mean absolute error (MAE) and mean square error (MSE), summarized in Table 1.

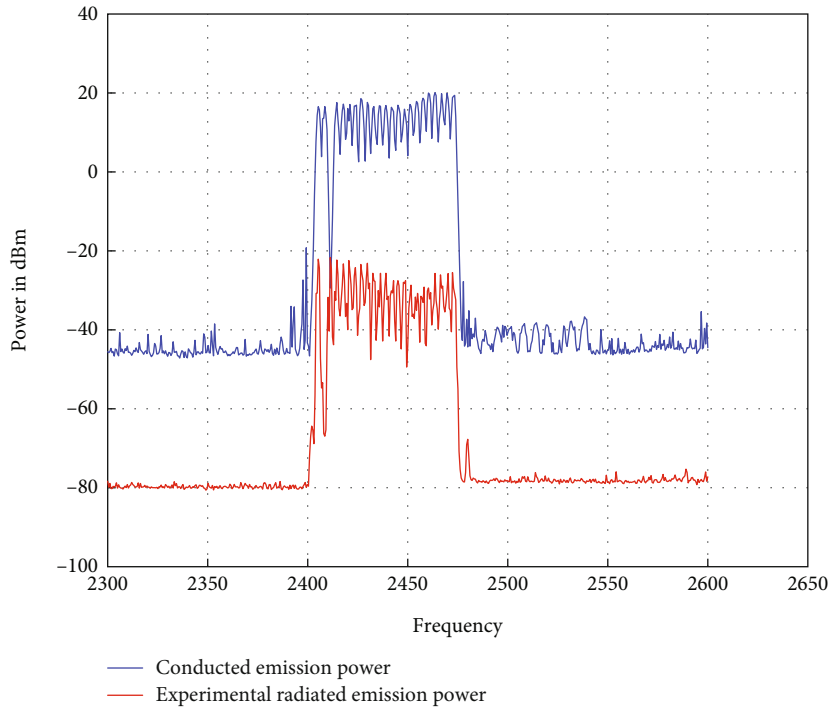

Figure 7: Conducted emission vs. radiated emission in the basement.

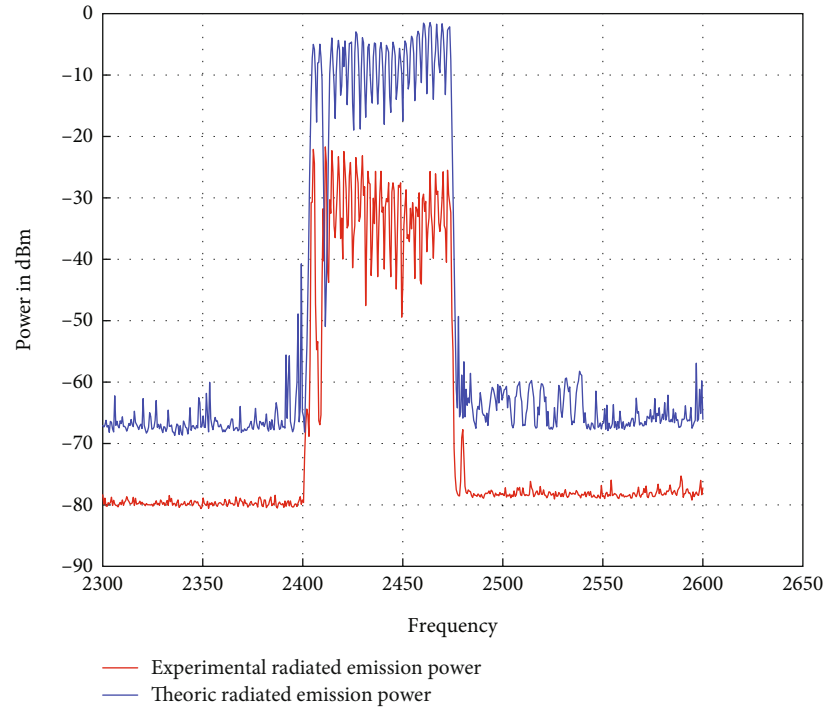

Figure 8: Radiated emission vs. theoretic radiated emission after considering only path loss attenuation in the basement.

Table 1 provides a comparative analysis of location-based error metrics, mean square error (MSE) and mean absolute error (MAE), both expressed in decibels (dB) for the theoretical model's calculation of a received signal against an experimental model. These metrics are computed using 551 samples within a bandwidth ranging from 2300 MHz to 2600 MHz across various environments: basement, open area, and forest.

In the basement environment, the MAE is the highest at 6.66 dB, indicating a moderate level of average absolute deviation from the actual measurements. This suggests that the theoretical model tends to be less accurate in the basement

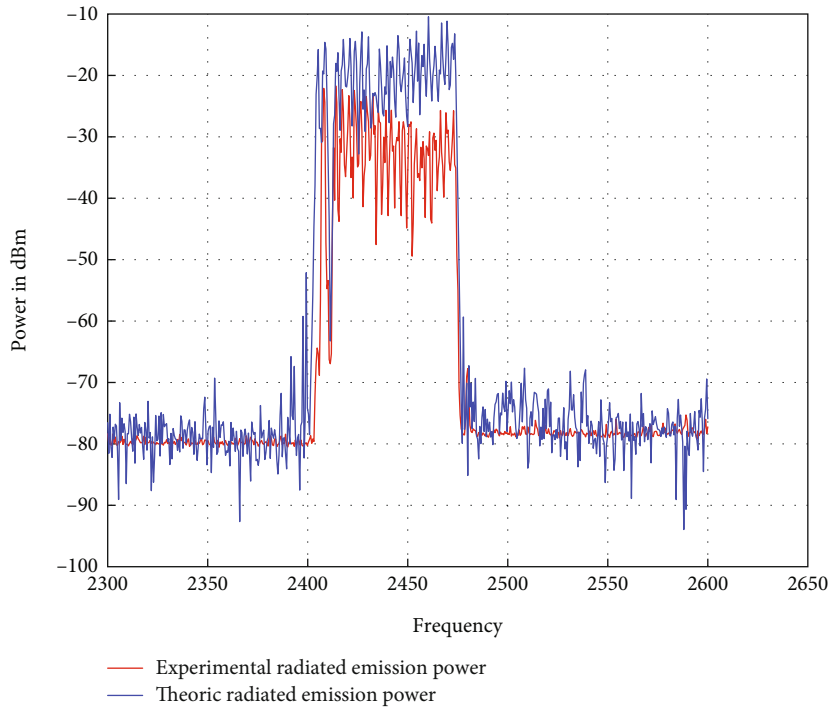

Figure 9: Experimental RE vs. theoretic RE after considering path loss, Rician channel, and AWGN channel in the basement.

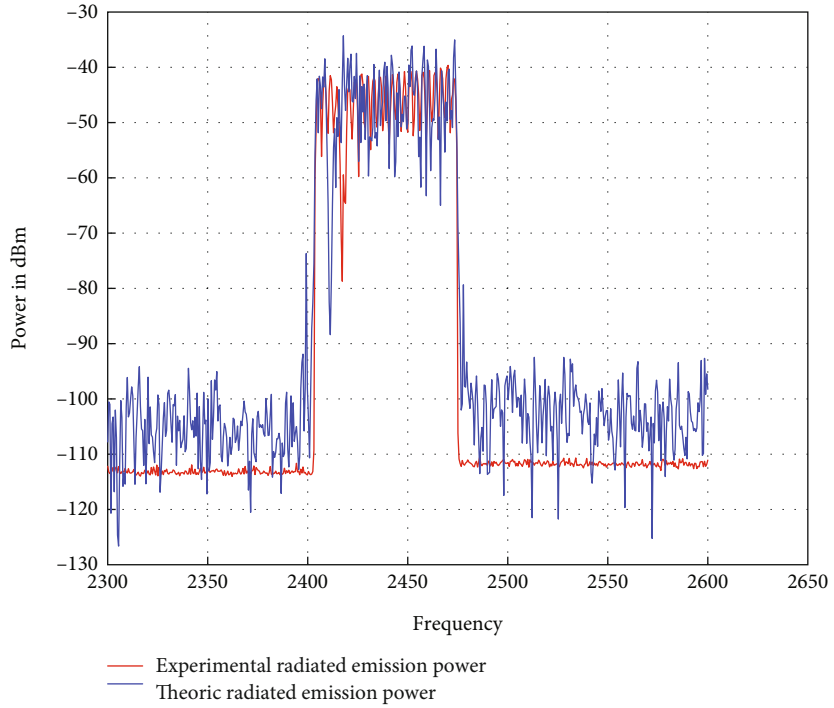

Figure 10: Experimental RE vs. theoretic RE after considering path loss, Rician channel, and AWGN channel in the forest.

setting. The MSE is also quite high at 90.87 dB, pointing towards larger errors and possibly a few extreme deviations, which significantly affect the model's predictive accuracy in this environment.

In the forest environment, the MAE is slightly lower than the basement at 6.40 dB but still indicates substantial average errors, which may be due to the complex signal propagation conditions typically found in forested areas.

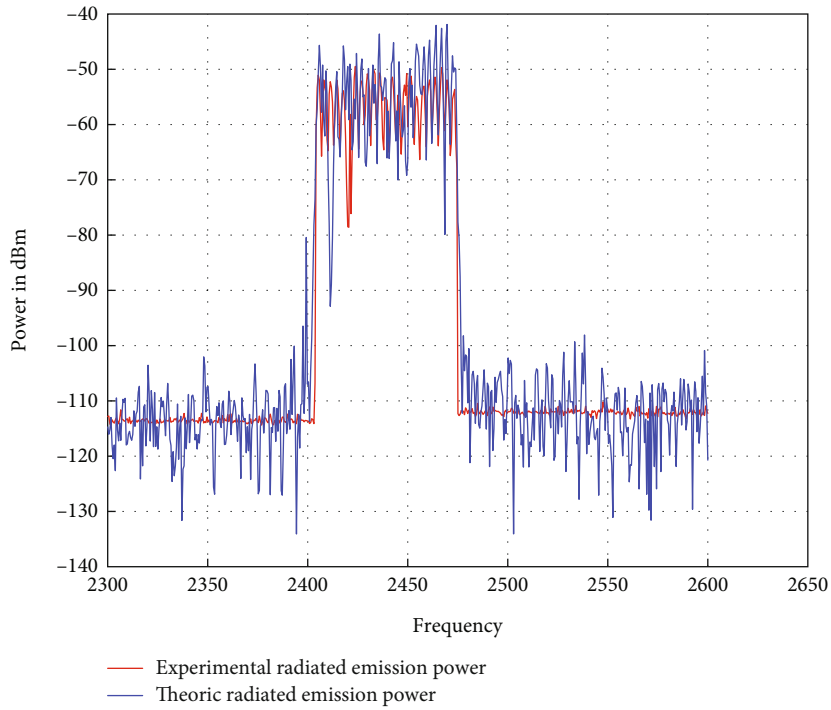

Figure 11: Experimental RE vs. theoretic RE after considering path loss, Rician channel, and AWGN channel in the open area.

Table 1: Comparative analysis of location-based error metrics across different environments using Monte Carlo simulation.

	Basement	Forest	Open area
MAE (dB)	6.658304	6.400293	5.395559
MSE (dB)	90.869257	82.337156	61.115936

The MSE is 82.33 dB, indicating that while the average errors are smaller than in the basement, there are still significant deviations from the actual values, reflecting the challenging nature of accurately modeling signal behavior in a forest environment.

In the open area environment, the MAE shows the lowest error at 5.39 dB, suggesting that the theoretical model is more accurate in open areas, which typically have fewer obstructions and a clearer line-of-sight for signal propagation. The MSE is significantly lower at 61.12 dB, implying fewer large errors and a higher overall accuracy of the model in open area conditions compared to the other environments.

It is important to highlight in this context that the experimentally measured signal underwent several processing steps within the frequency analyzer to achieve the smooth curve that is presented. Among these processing steps, the use of filters such as RBW (resolution bandwidth filters), VBW (video bandwidth filters), and antialiasing filters should be noted. This processing substantially accounts for the significant discrepancy observed in the mean square error (MSE) values.

The developed model intentionally omitted the consideration of filtering effects due to the unspecified behavior of the spectrum analyzer's filters within our specific context. Our primary objective centers on forecasting the influence of a particular environment on the drone's datalink through the application of mean absolute error (MAE) metrics. This focus led to the oversight of incorporating the signal processing parameters of the frequency analyzer, as evidenced by the elevated mean squared error (MSE) values.

In summary, the model has been successfully tested in 3 environments where the transmitted signal presents a strong LOS component compared to the scattered component:

(i) In the transmission scenario in the first environment, inside the basement room, several types of multipath fading can occur due to the specific environmental characteristics, such as limited space, walls, floors, ceilings, and possibly the presence of various objects. These conditions lead to different paths that the signal can travel from the transmitter to the receiver (4 m), yet Rician fading remains applicable, with the highest MAE (mean absolute error) value

(ii) In the forest environment, the signal is still in LOS with trees around. Even with greater distance between the transmitter and the receiver, the MAE metric is less than for the basement. We can explain that by the reduction of scattered paths reflected on the trees and the absence of ceiling and rebars in all the walls of the basement

(iii) In the open area, the situation is closely similar to the OATS. The signal in these kinds of sites has

reduced reflection paths, which explains the good MAE metric

5. Conclusion

The control of a drone through radio communication involves various attenuations caused by the operational environment. Frequency-hopping modulation provides transmitted signal robustness against jamming and attenuation. Despite this, the signal is strongly affected by its environment, consequently reducing its performance in terms of the drone control range and electromagnetic susceptibility.

This study presents a new model for estimating the received signal by modeling the operational environment. This model considers various attenuations suffered by the signal owing to large-scale and small-scale fading.

Considering the path loss fading (deterministic method) as well as the multipath fading and the additional white Gaussian noise (stochastic method), it allows the generation of a highly appreciable estimation of the received signal in the radiated mode. It is crucial to highlight the model's limitation due to its reliance on a strong line-of-sight (LOS) component for accurately modeling the real-world variability in signal strength across diverse environmental conditions.

The Monte Carlo simulation, integral to our analysis, indicates that while the model excels in open areas, it also performs commendably in forest and basement environments, showing a reasonable degree of accuracy as reflected by the MAE value. The simulation's extensive iterations confirm the model's robustness across diverse environmental conditions, successfully capturing the complex dynamics of signal attenuation and propagation, including the effects of small-scale fading.

This estimation can be used to assess the communication range between the ground control station and drone based on the transmitter's emitted power and environmental characteristics. Thus, we can use other parameters such as bit error rate in order to quantify the effectiveness of the datalink. Additionally, electromagnetic susceptibility can be improved by installing active filters according to environmental characteristics.

Finally, several improvements can be made to the model to improve the accuracy of predicting the radiated signal based on the conducted measurements and the environment characteristics.

The model's performance can be enhanced by incorporating additional communication configurations between the drone and the ground station. This includes accounting for the Doppler effect resulting from the drone's motion, the shadowing phenomenon that occurs when objects obstruct the path between the communication antennas (transmitter and receiver), and the impact of various noise sources. These noise sources could include proximity to high-voltage power lines or operating within urban areas characterized by a high electromagnetic spectrum density. By addressing these factors, the model can offer a more accurate and reliable prediction of communication performance under diverse environmental conditions.

Future research will focus on studying the impact of the environment on the datalink of a fixed-wing drone in dynamic flight. We plan to predict the range of the drone with the datalink in the considered environment. The research outcomes could contribute to the development of specific areas within drone communication systems. These areas include, for example, enhancing the reliability of communications, analyzing signal propagation under specific conditions, optimizing communication protocols, and employing artificial intelligence for improved decision-making and efficiency.

Data Availability

Data in the form of Excel sheet measurements and MATLAB code used in this study are available from the corresponding author upon request.

Conflicts of Interest

The authors declare that there is no conflict of interest regarding the publication of this paper.

Acknowledgments

All costs associated with the research and publication have been individually supported by the first author.

References

[1] G. Sadeque, S. C. Mohonta, and F. Ali, "Multipath Rayleigh and Rician fading channel simulation using MATLAB," *American Journal of Engineering Research (AJER)*, vol. 4, no. 6, pp. 36–42, 2015.

[2] J. Ma and H. Liu, "Performance analysis and simulation of UAV data link and communication link," in *Proceedings of the 2018 International Conference on Network, Communication, Computer Engineering (NCCE 2018)*, vol. 147, pp. 1024–1030, Atlantis Press, 2018.

[3] G. Wu, F. Li, and H. Jiang, "Analysis of multipath fading and Doppler effect with multiple reconfigurable intelligent surfaces in mobile wireless networks," *Wireless Communications and Mobile Computing*, vol. 2022, Article ID 5751316, 15 pages, 2022.

[4] C. T. Liu, R. J. Wu, Z. X. He, X. F. Zhao, H. C. Li, and P. Z. Wang, "Modeling and analyzing interference signal in a complex electromagnetic environment," *EURASIP Journal on Wireless Communications and Networking*, vol. 2016, 9 pages, 2016.

[5] H. Zhang, T. Li, Y. Li, and Z. Wen, "Virtual electromagnetic environment modeling based data augmentation for drone signal identification," *Journal of Information and Intelligence*, vol. 1, no. 4, pp. 308–320, 2023.

[6] R. Liao, H. Wen, J. Wu, H. Song, F. Pan, and L. Dong, "The Rayleigh fading channel prediction via deep learning," *Wireless Communications and Mobile Computing*, vol. 2018, Article ID 6497340, 11 pages, 2018.

[7] M. Petkovic and M. Narandzic, "Overview of UAV based free-space optical communication systems," in *Interactive Collaborative Robotics. ICR 2019*, A. Ronzhin, G. Rigoll,

and R. Meshcheryakov, Eds., vol. 11659 of Lecture Notes in Computer Science(), Springer, Cham, 2019.

[8] M. Najafi, H. Ajam, V. Jamali, P. D. Diamantoulakis, G. K. Karagiannidis, and R. Schober, "Statistical modeling of FSO fronthaul channel for drone-based networks," in *2018 IEEE International Conference on Communications (ICC)*, pp. 1–7, Kansas City, MO, USA, 2018.

[9] B. B. Yousif and E. E. Elsayed, "Performance enhancement of an orbital-angular-momentum-multiplexed free-space optical link under atmospheric turbulence effects using spatial-mode multiplexing and hybrid diversity based on adaptive MIMO equalization," *IEEE Access*, vol. 7, pp. 84401–84412, 2019.

[10] B. B. Yousif, E. E. Elsayed, and M. M. Alzalabani, "Atmospheric turbulence mitigation using spatial mode multiplexing and modified pulse position modulation in hybrid RF/FSO orbital-angular-momentum multiplexed based on MIMO wireless communications system," *Optics Communications*, vol. 436, pp. 197–208, 2019.

[11] N. Moraitis, K. Psychogios, and A. D. Panagopoulos, "A survey of path loss prediction and channel models for unmanned aerial systems for system-level simulations," *Sensors*, vol. 23, no. 10, p. 4775, 2023.

[12] S. Kaddouri, M. E. Hajj, G. Zaharia, and G. E. Zein, "Indoor path loss measurements and modeling in an open-space office at 2.4 GHz and 5.8 GHz in the presence of people," in *2018 IEEE 29th Annual International Symposium on Personal, Indoor and Mobile Radio Communications (PIMRC)*, pp. 1–7, Bologna, Italy, 2018.

[13] M. R. Hayal, E. E. Elsayed, D. Kakati et al., "Modeling and investigation on the performance enhancement of hovering UAV-based FSO relay optical wireless communication systems under pointing errors and atmospheric turbulence effects," *Optical and Quantum Electronics*, vol. 55, no. 7, p. 625, 2023.

[14] L. Bing, "Study on modeling of communication channel of UAV," *Procedia Computer Science*, vol. 107, pp. 550–557, 2017.

[15] M. B. Perotoni, R. D. P. de Araújo, and C. A. F. Sartori, "Unmanned aerial vehicle propagation datalink tool based on a hybrid multiscale modeling," *Journal of Aerospace Technology and Management*, vol. 10, 2018.

[16] D. Aláez, M. Celaya-Echarri, L. Azpilicueta, and J. Villadangos, "UAVradio: radio link path loss estimation for UAVs," *SoftwareX*, vol. 25, 2024.

[17] T. M. Macnamara, *Handbook of Antennas for EMC Second Edition*, vol. 4, Artech House, 2016.

[18] I. Bennageh, H. Mahmoudi, and M. Labbadi, "Impact of the electromagnetic environment on UAV's datalink," *IOP Conference Series: Earth and Environmental Science*, vol. 785, article 012010, pp. 1–6, 2021.

[19] Y. Li, Q. Ding, K. Li, S. Valtchev, S. Li, and L. Yin, "A survey of electromagnetic influence on UAVs from an EHV power converter stations and possible countermeasures," *Electronics*, vol. 10, no. 6, pp. 701–718, 2021.

[20] D. Tse and V. Pramod, *Fundamentals of Wireless Communication*, Cambridge University Press, 2012.

[21] G. Wang and H. Miao, "UAV data link system a survey," *Scientific Journal of Intelligent Systems Research*, vol. 3, no. 11, p. 10, 2021.

[22] M. Zolanvari, R. Jain, and T. Salman, "Potential data link candidates for civilian unmanned aircraft systems: a survey," *IEEE Communications Surveys and Tutorials*, vol. 22, no. 1, pp. 292–319, 2020.

[23] M. Strasser, B. Danev, and S. Čapkun, "Detection of reactive jamming in sensor networks," *ACM Transactions on Sensor Networks*, vol. 7, no. 2, pp. 1–29, 2010.

[24] United States Department of Defence, *MIL-STD-461G, Requirements for the Control of Electromagnetic Interference Characteristics of Subsystems and Equipment*, MIL-STD-461G, 2015.

[25] T. Kaur, J. Singh, and A. Sharma, "Simulative analysis of Rayleigh and Rician fading channel model and its mitigation," in *2017 8th International Conference on Computing, Communication and Networking Technologies (ICCCNT)*, pp. 1–6, Delhi, India, 2017.

[26] E. Bjornson and B. Ottersten, "A framework for training-based estimation in arbitrarily correlated Rician MIMO channels with Rician disturbance," *IEEE Transactions on Signal Processing*, vol. 58, no. 3, pp. 1807–1820, 2010.

[27] A. Tkac, V. Wieser, and S. Pollak, "Calculation of impulse response in Rician and Rayleigh channel," in *2012 ELEKTRO*, pp. 99–102, Rajecke Teplice, Slovakia, 2012.

[28] Z. Li, W. Chen, Q. Wu, H. Cao, K. Wang, and J. Li, "Robust beamforming design and time allocation for IRS-assisted wireless powered communication networks," *IEEE Transactions on Communications*, vol. 70, no. 4, pp. 2838–2852, 2022.

[29] O. Ozdogan, E. Bjornson, and J. Zhang, "Performance of cell-free massive MIMO with Rician fading and phase shifts," *IEEE Transactions on Wireless Communications*, vol. 18, no. 11, pp. 5299–5315, 2019.

[30] C. Tepedelenlioglu, A. Abdi, and G. B. Giannakis, "The Ricean K factor: estimation and performance analysis," *IEEE Transactions on Wireless Communications*, vol. 2, no. 4, pp. 799–810, 2003.

[31] S. Mukherjee, S. S. Das, A. Chatterjee, and S. Chatterjee, "Analytical calculation of Rician K-factor for indoor wireless channel models," *IEEE Access*, vol. 5, no. 12, pp. 19194–19212, 2017.

[32] M. Alymani, M. H. Alhazmi, A. Almarhabi, H. Alhazmi, A. Samarkandi, and Y.-D. Yao, "Rician K-factor estimation using deep learning," in *2020 29th Wireless and Optical Communications Conference (WOCC)*, pp. 1–4, Newark, NJ, USA, 2020.

[33] J. Wang, Y. Cui, H. Sun et al., "K-factor estimation for wireless communications over Rician frequency-flat fading channels," *IEEE Wireless Communications Letters*, vol. 10, no. 9, pp. 2037–2040, 2021.

[34] M. Naseri and N. C. Beaulieu, "Fast simulation of additive generalized Gaussian noise environments," *IEEE Communications Letters*, vol. 24, no. 8, pp. 1651–1654, 2020.